IEEE Access
Multidisciplinary | Rapid Review | Open Access Journal

Received 14 March 2025, accepted 15 April 2025, date of publication 28 April 2025, date of current version 5 May 2025.

Digital Object Identifier 10.1109/ACCESS.2025.3564636

RESEARCH ARTICLE

Deep Learning-Based Control of Active Power Filters Using LSTM and GRU Networks for Harmonic and Frequency Estimation

JUAN L. FLORES-GARRIDO[1], PATRICIO SALMERÓN[1], JUAN A. GÓMEZ-GALÁN[2], AND ALEJANDRO PÉREZ-VALLÉS[1]

[1]Department of Electrical and Thermal Engineering, University of Huelva, 21007 Huelva, Spain
[2]Department of Electronic Engineering, Computers and Automation, University of Huelva, 21007 Huelva, Spain

Corresponding author: Juan A. Gómez-Galán (jgalan@diesia.uhu.es)

ABSTRACT Deep Learning (DL) techniques provide a powerful tool enhancing the learning capabilities of the neural networks (NN), and are increasingly applied in the field of electric power systems. In particular, the long short-term memory (LSTM) and the gated recurrent unit (GRU) networks allow improvements on signal processing. The relevance of suppressing electrical disturbances justifies the efforts to apply new control algorithms to the active power filters (APF). Despite the existence of many control techniques, the NN-based proposals generally present significant shortcomings. Therefore, in this work, a new neural controller is presented for further improvement, using previously trained NNs, without need of adaptive algorithms. The generation of the three-phase APF reference currents is based on LSTM and GRU networks, that extract the full necessary information from currents and voltages, thus avoiding the need of an additional phase synchronization control. It is a novel proposal comprising FCE (fundamental Fourier coefficients estimation) and FE (frequency estimation) along with a simple computation process, for harmonic distortion and reactive power compensation. It has been tested with many practical loads and conditions through simulation and experimental platforms. Its general high performance confirms a substantial progress compared to other NN controllers, and it could be an alternative to other techniques.

INDEX TERMS Deep learning, long short-term memory (LSTM), gate recurrent unit (GRU), harmonic compensation, active power filter, artificial neural network, harmonic estimation, frequency estimation.

I. INTRODUCTION

In the last decade, the Deep Learning techniques, DL, have become a reference framework for many data processing and control systems applications. Therefore, it is mandatory to test their potential contribution in many engineering works, and especially in any tasks in which the classical artificial neural networks (ANN), were proven useful. The relevance of the electric power quality, EPQ, justifies the past and present struggle against electrical disturbances, which has led to the recent strong interest in DL applications for detection and correction of the EPQ problems. It is well known that the active power filter, APF, is a valuable device for mitigation of the poor quality of electrical waveforms [1], [2]. Although numerous technological advances and novel control methods were developed long ago enhancing the APF practical application, any innovative control strategy is still welcome. Convolutional networks, CNN, and the new generation of recurrent neural networks based on memory cells, such as the long short-term memory, LSTM, and the gated recurrent unit, GRU, provide a workbench full of improvement opportunities. Hence many DL-based control proposals are ongoing emerging in this particular area. Furthermore, in the general field of electric power systems, the widespread research proposing DL contributions has even given rise to review articles analyzing the state of the art and trends [3], [4].

The shunt APF consists of an electronic power converter for use in three-phase systems connected in parallel with the

The associate editor coordinating the review of this manuscript and approving it for publication was Muhammad Sharif.

load to supply compensation currents. The APF controller involves four main control areas [2], [5]. Firstly, the generation of reference currents required by the compensation purposes, encompassing one or more of the following goals: harmonic distortion mitigation, load reactive power compensation, and addressing the load currents imbalance. Then, the electronic converter requires a pulse width modulation technique (PWM) and its control system, as can be the usual hysteresis band (HB), to find the appropriate trigger pulses to switch the on-off states of the electronic power devices. The switching pulses and a local current control loop ensure the injection of currents according to the reference signals. A third control element that may be required is the phase synchronization technique [6], such as the usual phase-locked loop (PLL). Finally, the dc-voltage of the APF capacitors requires certain control techniques, such as the conventional PI regulation.

Regarding the reference current extraction, numerous techniques have been developed over the years and different classifications can be made [5], [7]. Two of the usual and relevant kinds of algorithms are based on the instantaneous reactive power theory (p-q) and the synchronous reference frame theory (SRF, d-q). The first one is considered a conventional technique, easy to implement. But they present the drawback of poor performance under conditions of source voltage distortion or imbalance [5], [8]. The SRF-based proposals generally combine frequency filters with a phase synchronization control. They are often used and some of them present good general results, as the Savitzky-Golay filter proposed in [8]. Other similar filter-based proposals seem to be very efficient [9], [10], [11], although some minor drawbacks may be observed. The work in [9] lacks sufficient validation with practical cases; the method with Kalman filter used in [10] is robust under different conditions but may be sensitive to the selection of weighting functions; and the proposal in [11] using a Wiener filter requires an iterative algorithm that is dependent on manually tuned parameters.

Another important group of control algorithms is based on the application of neural networks. The ANNs could provide efficient solutions due to their low latency and high capability for modelling complex nonlinear functions directly from patterns. However, most of the neural methods successfully used for the reference currents are based on adaptive techniques such as the least mean square (LMS). The adaptive ANN algorithms require rather high computation during the control execution and usually need a careful adjustment of the learning rate parameter. Whereas ANNs with only previous training could provide a more direct and fast response. The Adaline network is the main adaptive topology used in the proposals claiming good compensation results [12], [13], [14]. The work in [15] proposed an adaptive application of a radial basis function (RBF) network to enhance the PQ technique, although it was only applied to a single-phase system. The recurrent neural networks (RNN) have also been applied in some proposals, mostly combined with different adaptive algorithms [16], [17]. The method in [17] is supported by a wide variety of practical cases but is based on a high complexity algorithm.

On the other hand, there are few works proving that ANNs with previous training play the main role in the reference currents generation. The multilayer perceptron network (MLP) was compared to other neural techniques in [18] concluding that it did not perform as well as the Adaline methods. However, the more recent proposal in [19], with a previously trained MLP, was proven efficient to extract the fundamental harmonic of currents and voltages for easily computing the APF reference signals, although it needs the PLL synchronization.

In recent years, the development of DL techniques has provided a large advance in learning capabilities, providing a breakthrough in the application of the new neural networks. In the field of electric power systems some of the relevant areas of application are the following: classification of electric disturbances [20], power load forecasting [21], harmonic estimation [22], [23], and compensation control methods [24], [25], [26], [27]. The proposal in [24] presents the feasibility of CNN-LSTM architectures for harmonic prediction to know in advance a short time interval of the forthcoming current, which could improve the response time of an APF. However, no results of practical application are reported. The approach in [25] presents a LSTM-fuzzy control, tested in a single-phase active filter. The works in [26] and [27] present three-phase controllers based on GRU and LSTM, respectively, and seem to obtain good compensation results by simulated practical cases. Nevertheless, both publications contain scarce information about the training and the methods. In conclusion, there is not enough evidence of harnessing the new learning algorithms by the APF control.

In view of the above, a further comparative analysis of the cited neural techniques is conducted in the last section of this paper. Although there are efficient non-neural techniques available for the shunt APF control, generally the neural network (NN) solutions seem to present more shortcomings. It is apparent that further improvement could be made in these control techniques, especially in the use of previously trained NNs. Therefore, the aim of this work was to take advantage of the new DL tools to propose a new neural control method.

In this paper, a different and relatively simple control method is proposed for three-phase shunt APFs compensating harmonic distortion and reactive power. Previously trained NNs extract the full necessary information from the voltages and currents for generation of reference currents. The load currents imbalance can be corrected, in case of balanced supply voltages. It does not address this correction under unbalanced voltage conditions. The international standards have been considered regarding the possible grid frequency deviations (at least the interval $50\pm1\%$ Hz), the voltage harmonic distortion, and the recommended harmonic reduction rates. LSTM and GRU networks implement fundamental harmonic coefficients estimation, FCE, and a novel

frequency estimation function, FE. A quite straightforward procedure allows to generate the APF reference currents. The proposal has been widely tested with practical cases, providing high performance. The main contributions of this research are the following:

1) A method is presented for further progress in the application scope of previously trained ANNs to the APF control, with their typical low latency feature.
2) It is a novel proposal based on fundamental harmonic coefficients estimation, FCE, and grid frequency estimation, FE, implemented by LSTM and GRU networks, that avoids the need of a PLL.
3) It consists in a simple method for reference current generation, neither depending of the conventional transformations such as p-q or d-q, nor needing adaptive algorithms.
4) Fully detailed description of the training process is given. And a wide range of practical cases were tested to validate its general compensation qualities.

The paper has been structured as follows. Section II addresses the fundamentals of the control method. In Section III the LSTM and GRU networks are described. Section IV describes the training process to obtain the suitable NNs. Section VI contains the simulation results of practical cases. And Section VII comprises the experimental results with an APF prototype and a comparative discussion.

II. PROPOSED METHODOLOGY

A. MOTIVATION AND OBJECTIVES

Fig. 1 shows a three-phase system with a shunt APF injecting compensation currents according to the reference signals produced by, for example, a NN controller. The features of the compensation currents, i_C, depend on the kind of power quality improvement pursued, while verifying Kirchhoff's currents law.

$$i_S = i_L - i_C \tag{1}$$

Although some APF controllers are limited to the harmonic mitigation, it is more common to address, in addition, the reactive power compensation and the imbalance correction. As it was discussed in the previous section, there exist many different proposals, and some publications claim the validity of NN algorithms. However, they usually present one or another limitation or drawback. In the final section of this paper, where a comparative discussion is made, Table 11 collects relevant features of several notable works. There, it becomes clearer that the developed neural methods may still be further improved. In some cases, it is due to the insufficient compensation issues addressed [13], [14], and other proposals lack enough proven robustness or efficiency under certain conditions [12], [17], [26], [27].

In this work, the compensation objectives will be mitigation of load current harmonics and load reactive power, along with balancing the currents in most practical conditions. An additional requirement considered, to comply with the standards, is ensuring the APF performance in real distributions networks, where voltage distortion and frequency deviations can be present. A control proposal based on previously trained NN will require extensive training with variable fundamental frequencies within an interval around the nominal 50 Hz value. At least, the range between 49.5 and 50.5 Hz must be well addressed, according to the international standard IEC 61000-4-30 [28]. Moreover, from the requirements in the standard EN-50160 [29], the compensation equipment should be robust to harmonic distorted voltage and should satisfy the recommendation of producing source currents with total harmonic distortion (THD) below 5%.

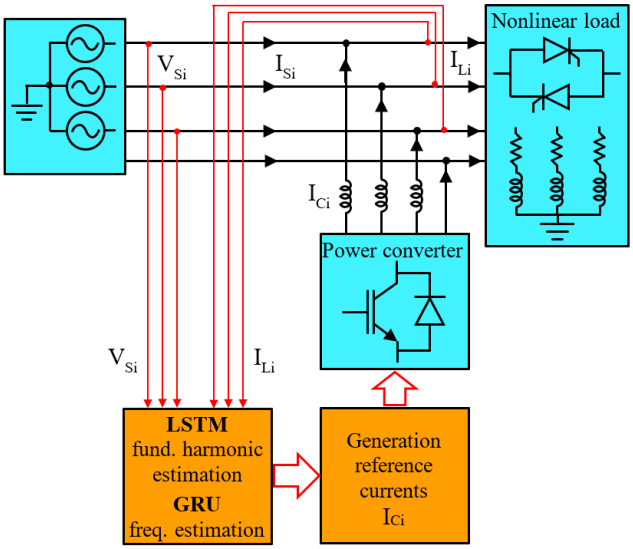

FIGURE 1. Three-phase system with shunt APF connected for compensation. Proposed DL-based control.

Besides, the typical dependency of many controllers on a phase synchronization technique such as the PLL, led us to propose a neural method comprising this function. Thus, the reference signals for the present APF control will be obtained through a two-step method. In a first stage, the currents and voltages must be acquired with a determined sampling rate, and the proposed DL networks must be able to estimate the features of the fundamental harmonic component of the different waveforms. It must work efficiently with all kinds of distorted waveforms and grid frequency deviations. The main parameters in a sinusoidal waveform are amplitude, phase, and frequency. An alternative way to know amplitude and phase information is determining the rectangular components coefficients of the sine function. Hence the first stage consists in the use of trained NNs to estimate the fundamental harmonic coefficients and the electric frequency. Regarding frequency estimation, the work in [30] reports using a feed-forward ANN approach to obtain the frequency by single tone sinusoidal communication signals. That application helped us decide to try it with harmonic distorted signals.

In a second stage, the resulting coefficients and frequency will be combined in a determined way to allow generating

the three-phase active currents signals. They are the desired source currents supplying the load active power and in phase with the fundamental harmonic of the supply voltage. For each phase, the difference between load and active currents gives the APF reference waveform. Fig. 1 illustrates this 2-stage separation of the method. The analytical foundations of the applied compensation strategy will be established in the following subsections.

B. FUNDAMENTAL RECTANGULAR COEFFICIENTS AND ACTIVE POWER COMPUTATION

It is well known that the waveform of a distorted current can be represented by the sum of different sinusoidal components with frequencies that are multiples of the fundamental one. Equation (2) shows the expression for a generic phase current of a nonlinear load, where the subscript $i = a, b, c$ represents the different phases, with $I_{h,i}$ and $\varphi_{h,i}$ being the *rms* values and phase angles, respectively, of the different harmonics.

$$i_{L,i}(t) = \sqrt{2}\, I_{1,i}\, \cos\left(\omega t - \varphi_{1,i}\right) + \sqrt{2} \sum_{\forall\, h\geq 2} I_{h,i}\, \cos\left(h\,\omega t - \varphi_{h,i}\right) \quad (2)$$

The first term in (2) is the fundamental harmonic of the load current, $i_{L1,i}(t)$, shown in (3). It is a sinusoidal waveform with a certain amplitude and phase angle.

$$i_{L1,i}(t) = \sqrt{2}\, I_{1,i}\, \cos\left(\omega t - \varphi_{1,i}\right) \quad (3)$$

The sinusoidal waveform (3) can also be expressed through its rectangular components (4), as the sum of two terms,

$$\begin{aligned} i_{L1,i}(t) &= \sqrt{2} I_{1,i}\, \cos\varphi_{1,i} \cos\omega t + \sqrt{2} I_{1,i}\, \sin\varphi_{1,i} \sin\omega t \\ &= A_{I,i} \cos\omega t + B_{I,i} \sin\omega t \end{aligned} \quad (4)$$

where $A_{I,i}$ and $B_{I,i}$ are real numbers representing the fundamental harmonic rectangular coefficients, of any phase current, and may easily be related to the amplitude and phase angle. Therefore, both pairs of parameters contain the essential information of a sinusoidal waveform at a given frequency.

In the same way, the source voltage waveforms can be split into the fundamental component and harmonic distortion components. Moreover, if we assume a pure sinusoidal voltage, there would be only the fundamental frequency component given by (5).

$$v_i(t) = A_{Vi} \cos\omega t + B_{Vi} \sin\omega t \quad (5)$$

where $A_{V,i}$ and $B_{V,i}$ are the coefficients of any phase voltage waveform, as described in (4) for the load current.

The estimation of the coefficients of voltage and current waveforms in each phase will allow establishing reference currents for the shunt APF. However, as the electric frequency of the grid can suffer small deviations, it is convenient to accurately estimate its values. The generation of the appropriate APF reference waveforms requires this variable to be determined at any time.

A first magnitude to be computed from the coefficients is the active power. Here the supply voltage will be considered very low distorted, and hence a sinusoidal voltage will be assumed. From (4) and (5), the part of the instantaneous power of each phase that can contribute to the transfer of active power is $p_i(t)$,

$$\begin{aligned} p_i(t) &= v_i(t) \cdot i_i(t) \\ &= \left(A_{V_i} \cos\omega t + B_{Vi} \sin\omega t\right) \cdot \left(A_{Ii} \cos\omega t + B_{Ii} \sin\omega t\right) \end{aligned} \quad (6)$$

with $i = a, b, c$. The trigonometric manipulation of (6) allows to obtain (7),

$$\begin{aligned} p_i(t) = A_{Vi}A_{Ii} + \frac{A_{Vi}B_{Ii} + B_{Vi}A_{Ii}}{2} \sin 2\omega t \\ + \left(B_{Vi}B_{Ii} - A_{Vi}A_{Ii}\right) \sin^2 \omega t \end{aligned} \quad (7)$$

The active power for the phase 'i' is the average value of $p_i(t)$ over a period. This is,

$$P_i = \frac{1}{T} \int_0^T p_i(t)\, dt = \frac{A_{Vi}A_{Ii} + B_{Vi}B_{Ii}}{2} \quad (8)$$

In the three-phase system, the sum of the three active powers as in (8) gives the total active power, that will be a function of the coefficients, as in (9)

$$\begin{aligned} P = \frac{1}{2} \left(A_{Va}A_{Ia} + B_{Va}B_{Ia} + A_{Vb}A_{Ib} + B_{Vb}B_{Ib} \right. \\ \left. + A_{Vc}A_{Ic} + B_{Vc}B_{Ic}\right) \end{aligned} \quad (9)$$

Under the stipulated conditions (unbalanced/sinusoidal voltage, unbalanced/non-sinusoidal current) only the fundamental harmonics of voltage and current will be involved in the determination of (9).

C. COMPENSATION CURRENTS

The unit power factor (PF) objective will be achieved when the source current is in phase with the voltage, that is, the source supplies the so-called active current. This current is responsible for transferring the load active power. Hence, the phase currents of the source after compensation can be expressed as in (10).

$$i_{S,i}(t) = G\, v_i\,(t) \quad (10)$$

where G is the so-called equivalent conductance of the load, defined by (11).

$$G = \frac{P}{V^2} = \frac{P}{V_a^2 + V_b^2 + V_c^2} \quad (11)$$

That is, the load conductance G is the division of the active power and the squared *rms* value of the three-phase voltage, determined from the *rms* values of the phase voltages, V_i.

This *rms* value of the three-phase voltage can also be written as a function of the coefficients, since for each phase (12) is verified.

$$\sqrt{2}\, V_i = \sqrt{A_{Vi}^2 + B_{Vi}^2} \quad (12)$$

And therefore,

$$V^2 = \frac{1}{2}\left(A_{Va}^2 + B_{Va}^2 + A_{Vb}^2 + B_{Vb}^2 + A_{Vc}^2 + B_{Vc}^2\right) \quad (13)$$

From (9) and (13) G is obtained, as in (14). The computation of (14) involves the twelve coefficients.

$$G = \frac{A_{Va}A_{Ia} + B_{Va}B_{Ia} + A_{Vb}A_{Ib} + B_{Vb}B_{Ib} + A_{Vc}A_{Ic} + B_{Vc}B_{Ic}}{A_{Va}^2 + B_{Va}^2 + A_{Vb}^2 + B_{Vb}^2 + A_{Vc}^2 + B_{Vc}^2} \quad (14)$$

Finally, using the desired source current waveforms determined in (10), the compensation currents produced by the APF should be obtained as in (15),

$$i_{C,i}(t) = i_{L,i}(t) - G\, v_i(t) \quad (15)$$

These compensation currents will give rise to a unity source PF, with sinusoidal currents. The voltage $v_i(t)$ in (15) corresponds to (5). In practical conditions where the source voltage could present significant distortion, $v_i(t)$ will contain only its fundamental component, instead of exactly the real voltage waveform, since the harmonic suppression objective requires obtaining a sinusoidal source current.

A first overview of the control method can be summarized as follows. The data acquisition of voltage and current signals provides the inputs for the NNs, which take on the FCE and FE tasks. From the coefficients, the equivalent conductance G is computed. Using G and the frequency, the active phase currents are generated. Then, the subtraction shown in (15) gives the reference compensation currents. Fig. 2 and the next subsection show further details.

D. REFERENCE CURRENTS PROCESSING

In view of the above, the resulting method consists in the following. Equation (10) corresponds to the desired active currents necessary as reference waveforms. If we call them $i_{Lref\_i}(t)$, these reference currents are as follows:

$$i_{Lref\_i}(t) = G\, v_i(t) \quad (16)$$

Then, from (5) and (16) the reference signals will be computed as in (17), where it appears the voltage coefficients array,

$$\begin{pmatrix} i_{Lref\_a} \\ i_{Lref\_b} \\ i_{Lref\_c} \end{pmatrix} = G \begin{pmatrix} A_{Va} & B_{Va} \\ A_{Vb} & B_{Vb} \\ A_{Vc} & B_{Vc} \end{pmatrix} \begin{pmatrix} \cos(\omega t) \\ \sin(\omega t) \end{pmatrix} \quad (17)$$

The reference compensation currents for the APF, according to the subtraction given in (15), become:

$$\begin{pmatrix} i_{Cref\_a} \\ i_{Cref\_b} \\ i_{Cref\_c} \end{pmatrix} = \begin{pmatrix} i_{L\_a} \\ i_{L\_b} \\ i_{L\_c} \end{pmatrix} - G \begin{pmatrix} A_{Va} & B_{Va} \\ A_{Vb} & B_{Vb} \\ A_{Vc} & B_{Vc} \end{pmatrix} \begin{pmatrix} \cos(\omega t) \\ \sin(\omega t) \end{pmatrix} \quad (18)$$

where the conductance G is obtained as in (14) and involves both voltage and current coefficients. Equation (18) represents the essential features of the proposed method. These compensation waveforms needed for the PWM control of the power converter will lead to the injection of the appropriate compensation currents into the 3-phase system. Therefore, the proposal depends on the precise knowledge of the fundamental coefficients and the electric frequency. In Fig. 2, a flowchart of the control method is depicted, also including the earlier phase of NN training.

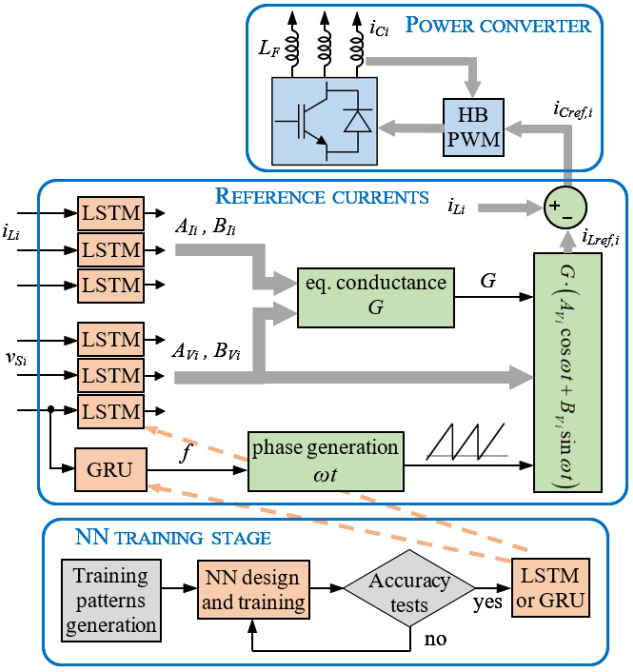

FIGURE 2. Flowchart of the control method.

A thorough implementation of the expression in (18) will cover the phase synchronization function, avoiding the use of a conventional PLL. It follows a description of the process ensuring the correct phase in the reference currents based on the estimated frequency. It requires a computation of ωt according to the data acquisition rate and the use of the NNs for FCE and FE. For a nominal 50 Hz frequency, the output values of coefficients and frequency will be updated every 20 ms cycle. The A and B coefficients will contain the phase angle information of every 20 ms window of the sampled signals. The ωt must be generated in a special way to take advantage of the estimated f. Let call t^* to a periodic time function running from 0 to 0.02 seconds that can be seen as a periodic ramp function with slope 1, or a sawtooth function (see Fig. 3).

This time t^* takes charge of the FCE and FE outputs rate, with update period of 0.02 seconds. But the actual electrical f could be different from the nominal value, f_o. Therefore, the computed phase must be:

$$\omega t = 2\pi f\, t^* + 2\pi f_0 \left(\frac{1}{f_0} - \frac{1}{f}\right) \quad (19)$$

Which can also be written, for $f_o = 50$ Hz, as follows:

$$\omega t = 2\pi f\, t^* + 100\pi \left(\frac{1}{50} - \frac{1}{f}\right) \quad (20)$$

These equations allow to obtain the ωt phase at the actual signal frequency using the f estimation and a constant-period repeating time [0, 0.02], synchronous with the updates of the acquisition and control system. The second term addresses the adjustment necessary to correct the small phase shift produced by the possible Δt time difference between the actual period T and the constant period 0.02 s of the control system. Fig. 3 depicts a schematic of the FE-based phase synchronization.

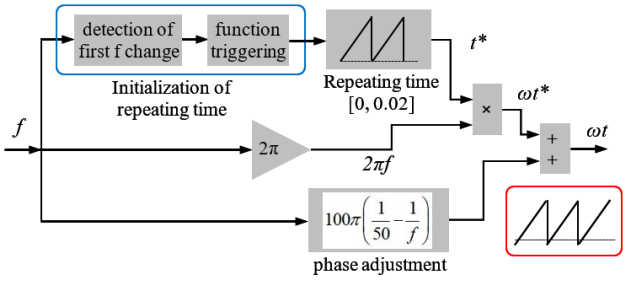

FIGURE 3. Diagram of the phase generation and synchronization.

At the start of the control system, the synchronization of the reference generation and the control running cycle requires an initialization of the repeating time t*, based on a detection of the first f change coming from the NN, that triggers the time ramp function. The product of 2π f and t* gives ωt^*, that needs the addition of the second term in (20) for the small correction when f $\neq$ 50 Hz. The resulting ωt provides the argument for the cosine and sine functions.

III. DEEP LEARNING FRAMEWORK FOR THE PROPOSED METHOD

Deep Learning is a set of methods based on using multi-layered neural networks, called deep neural networks, to simulate the complex decision-making potential of the human brain. Deep Learning comprises many network architectures, based on the connection of multiple layers for processing the input data. Different training algorithms are available for the learning process, adapted to the supervised/unsupervised learning, and to the diverse types of application tasks. The fundamentals of DL come from the ANN theories and methods but involve a wide extension of the concepts and methodologies, including numerous additional operations and algorithms.

The layers accomplish many different functions in the network. The DL *layer* concept does not mean only a set of artificial neurons, but instead it includes a variety of operations contributing to improve the different data-processing steps. Among the so-called neuronal layers, it comprises the classical ones and new processing modes that supported the enhanced learning power of DL: the convolutional layer, and new recurrent layer based on memory cells. The principal recurrent type is the long short-term memory layer (LSTM). A network based on convolutional layers is called convolutional neural network, CNN. And the network based on LSTM layers is called LSTM network. Among the CNNs, the most common type is the 2D-CNN, but it is also available the 1D-CNN, more appropriate for unidimensional signal processing. From the LSTM some important variants have been derived, with the common feature of recurrent memory cells. The gated recurrent unit network, GRU, is the most known.

The NN layers may be combined giving hybrid structures, such as CNN-LSTM, CNN-GRU or LSTM-GRU. It is usual, depending on the learning tasks, to test different configurations in the search of the best result. In this work, different network architectures have been used. Weather using one or another DL algorithm depended on the performance found with it. In this sense, as it will be justified in section IV, the CNN did not provide the expected performance. Therefore, in the next subsections we describe the DL models found useful in this application: LSTM and GRU networks.

A. LONG SHORT-TERM MEMORY NETWORKS

LSTM layers have some features common with the classical recurrent networks, RNN, because they contain feedback or recurrent connections. Instead of neurons, they are based on more complex processing units called cells. This kind of cell was designed in several steps along the years, trying to enable and improve the memory capabilities for time-variant data. Since the first version in 1997, the model was improved up to the current efficient structures. The cell architecture is depicted in Fig. 4. The LSTM layer contains a number of cells, ranging from few ones up to hundreds of them.

The cell owns two internal memory states that enhance the learning capacity by inputs presenting temporal dependency. They are the cell state, c_t, and the hidden state, h_t. The cell is made up of three components or gates to regulate the memory states through time: forget gate, input gate and output gate.

At some timestep t, the input vector x_t, together with the previous state values, h_{t-1} and c_{t-1}, are computed to yield new hidden and cell states, h_t and c_t. The cell output into the following network layer, y_t, is the same as h_t.

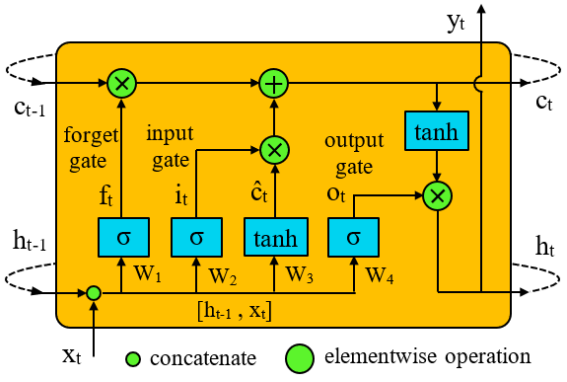

FIGURE 4. LSTM cell, showing its architecture and operation details.

Next follows firstly the mathematical operation description, and then a brief interpretation. The recurrent input

h_{t-1} and the data input vector x_t, after a concatenation, become the input vector of the 4 fully connected elements that work as typical artificial neurons. The weighted sum of the input elements, plus a typical bias value, gives the argument for the activation functions, sigmoid or tangent hyperbolic. As shown in (21) and in Fig. 4, four new magnitudes are obtained: the forget, the input, the ''candidate'', and the output. It is interesting to remark that the computations in (21) are just the operations of 4 neurons.

$$\begin{cases} f_t = \sigma\left(W_1 \cdot [h_{t-1}, x_t] + b_1\right) \\ i_t = \sigma\left(W_2 \cdot [h_{t-1}, x_t] + b_2\right) \\ \hat{c}_t = \tanh\left(W_3 \cdot [h_{t-1}, x_t] + b_3\right) \\ o_t = \sigma\left(W_4 \cdot [h_{t-1}, x_t] + b_4\right) \end{cases} \tag{21}$$

Then the addition of two products yields the new cell state c_t, as shown in (22). The update of the hidden state consists in the product of o_t and $tanh(c_t)$, as shown in (23). In these two equations, the addition and the product are usually assumed as ''elementwise'' operations to provide general and precise definitions of the cell computation. Thus, the cell mechanism rules are well-defined to embrace more complex cell configurations. However, by the cell description made here, that covers the commonly used LSTM networks, no special definitions must be considered for the addition and the product.

$$c_t = f_t \times c_{t-1} + i_t \times \hat{c}_t \tag{22}$$

$$h_t = o_t \times \tanh\left(c_t\right) \tag{23}$$

Finally, the new h_t value in (23) is used as cell output and as recurrent input for the next time step. The weights in vectors W_i and the biases b_i make up the set of adjustable parameters of the LSTM layer in the network training process.

A brief interpretation follows about the role of the three gates. Altogether the gates enable the cell to retain the important information from the past and discard the irrelevant one. The forget gate, with values between 0 and 1, determines which information to discard from the previous cell state. The tanh computation that gives the candidate $\hat{c}_t$, with values between -1 and 1, is a regulation of the influence magnitude of previous hidden state and current input to the cell state. The input gate i_t, with values between 0 and 1, controls the access of candidate values $\hat{c}_t$ to the cell state. The output gate, with values between 0 and 1, controls the portion of the cell state allowed to be transferred to the cell output, h_t or y_t. This value will be returned to the cell as input for the next time step.

At each time step, a new input x_t from a data sequence is used, both cell and hidden states are updated, and a new output y_t is obtained. This whole mechanism provides the LSTM cells with relatively long-time memory, which is called long short-term memory.

The training of LSTM networks consists in adjusting the weight matrix W and bias vector b of every cell, using a set of patterns, by means of a backpropagation algorithm. As an example of an LSTM network, Table 1 shows the layers and details of one of the networks employed in this work. It comprises an 80-cell layer and a 2-neuron fully connected layer. As every cell involve 4 neurons, it is easy to understand the number of weights shown in the table.

TABLE 1. Parameters of an 80-cell LSTM network used in this work.

Layers	Inputs	Outputs	N. of weights and biases
Sequence input	1	1	-
LSTM 80 cells	1	80	input weights 4×80 recurrent weights 4×80×80 biases 4×80
Fully connected	80	2	input weights 80×2 biases 2
Regression output	2	2	-

One remarkable detail observed in Table 1 is the number of recurrent weights appearing in this case, designed with MATLAB, that are $4 \times 80 \times 80$, which means that all hidden states of the 80 cells are used recurrently as input for every cell present in the layer.

B. GATED RECURRENT UNIT NETWORKS

The GRU network is similar to the LSTM, but it is based on a different cell mechanism. It was introduced in 2014 by K. H. Cho et al. [31]. The cell has two gates, which enables it to input and forget certain features. But it has neither an output gate nor a cell state, resulting in fewer parameters and variables. However, the GRU network has exhibited high performance in many applications, even higher than the LSTM in some cases. Therefore, when working with NNs based on memory cells it is convenient to test both LSTM and GRU, because any of them could achieve better performance, depending on the task.

Fig. 5 shows the GRU cell architecture, illustrating the operation with 2 gates, 3 neurons, and only one hidden state. At some timestep t, the cell computes the input vector x_t and the previous hidden state h_{t-1}, producing the new hidden state value h_t. The cell output into the next layer in the network, y_t, is the same as h_t.

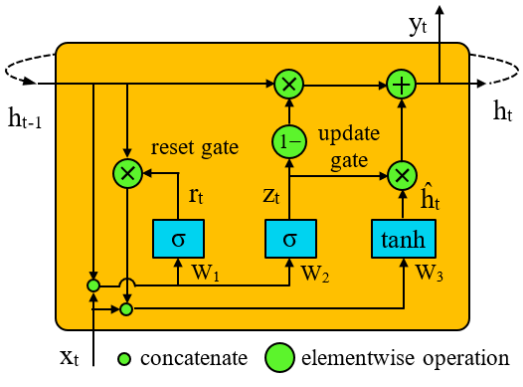

FIGURE 5. GRU cell, showing its architecture and operation details.

The recurrent input h_{t-1} and the data input vector x_t, after a concatenation, become the input vector of two neurons with log-sigmoid activation function. This yields the reset and update variables, r_t and z_t, according to (24).

$$\begin{cases} r_t = \sigma\left(W_1 \cdot [h_{t-1}, x_t] + b_1\right) \\ z_t = \sigma\left(W_2 \cdot [h_{t-1}, x_t] + b_2\right) \end{cases} \tag{24}$$

Another concatenated vector is made up, where h_{t-1} is first multiplied by the reset r_t, as shown in Fig. 5. This vector is the input of the third neuron, with *tanh* function, whose output is the candidate value $\hat{h}_t$, as shown in (25),

$$\hat{h}_t = \tanh\left(W_3 \cdot [r_t \times h_{t-1}, x_t] + b_3\right) \tag{25}$$

Finally, the new current hidden state h_t is obtained by addition of two terms, that represent two different contributions of the update z_t to the hidden state. It is shown in (26). Fig. 5 points out the additions and products that can be assumed elementwise operations, for better definition of the general rules in (25) and (26), in case of more complex cell configurations.

$$h_t = (1 - z_t) \times h_{t-1} + z_t \times \hat{h}_t \tag{26}$$

The reset gate r_t has values between 0 and 1, and it is multiplied with h_{t-1}. Hence this gate controls the portion of information in h_{t-1} that can be forgotten, and the portion that passes through for computation of the candidate value. The update gate z_t also has values between 0 and 1. Its role is to regulate the access of the candidate to the hidden state, deciding the proportions of the old hidden state and the current candidate to be added, generating the new h_t. This value will be returned to the cell as input for the next time step.

At each time step, a new input x_t from a data sequence is used, and a new output y_t is obtained. This mechanism provides the GRU cells with the same memory features as the LSTM. The training consists in adjusting the weight matrix W and the bias vector b of every cell. The GRU network requires a slightly lower computation amount than the LSTM.

IV. TRAINING THE NN FOR FCE AND FE

As stablished in Section II, the compensation reference currents can be obtained by determining the fundamental harmonic coefficients, A_i and B_i from the generally distorted current and voltage, as well as the actual grid frequency. The reference generation requires the precise estimation of coefficients and electric frequency at any time to avoid malfunction.

Different DL architectures including CNN, LSTM, GRU and biLSTM have been widely tested, both for FCE and FE tasks. However, the main models used in this research have been LSTM and GRU networks.

The software tool employed has been the MATLAB computing environment, including Simulink, the Deep Learning Toolbox and the Deep Network Designer App. The network design and the training work can be made through the graphical interface of the Deep Network Designer, or by means of code editing in MATLAB programming language. Both ways allow to develop the entire work process, comprising the combination of layers, the adjustment of hyperparameters, the selection of the previously prepared patterns database, and the configuration of the training algorithms.

A. TRAINING THE NN FOR FCE

With the aim of training NNs for FCE from distorted waveforms, a first decision to make was the convenient signal sampling rate. Many tests were carried out, checking the learning performance, with CNN and LSTM networks, using 64 points per cycle (20 ms period), 128, 256, and 512. The authors' previous experience with ANNs, along with the results obtained in the tests, led to the conclusion that 128 samples/cycle was sufficient in this application. Thus, as a compromise between extraction of enough signal information and moderated computation burden, a value of 128 samples per waveform cycle was chosen. Considering a nominal frequency of 50 Hz and period of 20 ms, the sampling rate was 6.4 kHz (k-samples/second).

1) GENERATION OF THE LEARNING PATTERNS

A big set of harmonically distorted waveforms is required as learning patterns. The selection of suitable magnitudes of the different harmonics is based on a thorough analysis of current harmonic spectrums by practical nonlinear loads along the trial-and-error. The set of learning patterns have included all possible phases between 0 and 360 degrees, by using both negative and positive A and B coefficients, according to (4). It is usual to apply neural techniques with normalized input signals, aiming to handle numbers not much beyond the [−1,1] interval, which may provide higher performance. Table 2 shows the parameter combinations for the generated pattern set. The odd order harmonics have been combined up to the 35th order, establishing decreasing value intervals for the different harmonics.

TABLE 2. Parameters in the set of learning patterns.

Coefficients	Training intervals	N. of steps	Freq. (Hz)	N. of patterns
A_1, B_1	[−1.5, 1.5]	21	49.5	40000
A, B_3	[−0.6, 0.6]	5	49.6	40000
A_5, B_5, A_7, B_7	[−0.4, 0.4]	5	...	...
A_9, B_9, A_{11}, B_{11}	[−0.2, 0.2]	3		
… …	…	…		
A_{35}, B_{35}	[−0.01, 0.01]	3	50.5	40000

As shown in Table 2, the patterns were prepared using different values of fundamental frequency between 49.5 and 50.5 Hz, distributed in steps of 0.1 Hz. That is, 11 different values. For every frequency an amount of 40 thousand waveforms, 20 ms long, were generated. The harmonic combination in each pattern was generated randomly, by means of the uniformly distributed discrete random function, *unidrnd* in MATLAB. For example, the first coefficient, A_1, takes

values according to (27).

$$A_1 = (unidrnd\ (21, 1, 1) - 11)^* 0.15 \tag{27}$$

Thus, a total of 440 thousand waveforms formed the learning base. The patterns, including the input waveforms and the $[A_1, B_1]$ target vectors, were structured as an *arraydatastore* for use as training database. Besides, a validation *arraydatastore* was generated with different patterns to use during the learning process. That format enhances the training computation by reading the patterns in every iteration at a suitable pace, corresponding to the minibatch size, which is a training parameter usually fixed as 100 or 128.

2) DNN CONFIGURATION AND TRAINING PROCESS

The first challenge in DL application is the NN architecture selection. Taking as a starting point the technical literature reviewed, followed by a trial-and-error analysis, it was progressively decided which models to discard and which NNs to further apply. Proposals based on CNNs, as in [22] and [23], led us to begin with convolutional networks, although some authors [21], [25], suggest better using approaches based on the LSTM for this kind of time varying signals.

A CNN architecture composed of two convolutional blocks, each one containing 3 layers (1DConv, tanh, max-pooling), and a final fully-connected layer, was widely tested. Nevertheless, we were not able to obtain good results with this NN type. Also, combinations CNN+LSTM were tested, but the best performance in our trials was found using simple LSTM or GRU networks. Once proven that LSTM could be correctly trained, we continued using memory cell models.

The biLSTM layer, a variant of the LSTM, was also tested. After a thorough comparison of both types, in general, the LSTM yielded better performance.

Among the multiple structures based on the LSTM layer, the simplest one was proven the best for the FCE task. A four-layer model as in the example of Table 1 was the choice. Taken apart the input and output layers, that do not involve neural processing units, the model simply consists of two main layers: A LSTM layer, and a 2-neuron fully-connected layer.

The NNs must be trained, and next applied for prediction, with inputs consisting in 1×128 vectors, giving a new output at the end of each cycle of 128 samples. These vectors can feed the NN in two ways: using an input layer of size 1 with a sequential input of the vector or using an input layer of size 128 with a simultaneous input of the full vector. Whether using one or another mode, it is not relevant for the proposed application to the electric waveforms in this approach, as the generation of the reference signals for the APF is based on detection of the fundamental harmonic component after every cycle. The use of the NN in both the simulation system and the experimental setup is done through a buffer retaining the cycle samples. Therefore, both input methods have been considered by the training, with the aim of selecting the best result.

The backpropagation training algorithm computes an error function as accuracy goal whose value must be minimized. Typically, this function is the mean squared error MSE of the outputs compared to the targets, although in the regression tasks in MATLAB the performance progress is displayed in terms of the Loss function and the RMSE, with the Loss being one half of the MSE. The RMSE is shown in (28). After computation of the error, the backwards part of the iteration adjusts the weights and biases of the network layers. Each iteration is applied with de number of patterns determined in the batch size parameter, adjusted usually at a value of 100.

$$RMSE = \sqrt{\frac{1}{m}\sum_{i=1}^{m} \|\mathbf{y}_i - \mathbf{t}_i\|^2} \tag{28}$$

In (28), m is the number of training patterns defined in the batch size, and $\boldsymbol{y_i}$, $\boldsymbol{t_i}$, are the output and target vectors corresponding to the pattern i. The difference $\boldsymbol{y_i}$-$\boldsymbol{t_i}$ is the error vector, and $\|\boldsymbol{y_i}$-$\boldsymbol{t_i}\|$ expresses the error vector length in the output space. The error function is applied to both the training patterns and the validation set throughout the training iterations. The performance index, in terms of Loss or RMSE applied to the validation set, is the main reference to evaluate the training results.

Regarding the hardware employed, it was a usual personal computer Intel® Core-i7, 16 GB DDR4 of RAM memory, without GPU. The trainings were executed in the CPU, and the training times were relatively short, around some minutes, always less than an hour. Longer training times did not produce better results. Table 3 summarizes the different parameter configurations of the LSTM and the training algorithm. The left part shows the main training features with clear influence in the results, and the best adjustment giving the lowest validation RMSE. The right part shows different numbers of cells in the LSTM layer, and the final RMSE in every case.

TABLE 3. Details of the LSTM hyperparameters and training options optimization process.

Parameters	Test set	Best	LSTM cells	RMSE
algorithm	sgdm, adam, rmsprop	sgdm	40	0.0075
learn. rate DF	0.001 - 0.5	0.01	60	0.0063
batch size	50, 80, 100, 128, 200	100	80	0.0056
epochs	5, 8, 10, 20	8-10	100	0.0058

From the results shown in the right part of Table 3, the final trained network was taken with 80 cells. Some other hyper-parameters, not present in the table, were not relevant, such as, for example, the weights-initializer type (zeros or random). Regarding the sequential or non-sequential mode for the input vectors, the details shown in Table 3 belong to the non-sequential case, with input layer size of 128. In the case of sequential input, it also worked, but with less accuracy. In that case, the *adam* algorithm was found to be the best,

and the other parameters were similar, except for a worse final error around RMSE = 0.02.

The performance of the trained networks from the different runs was further evaluated in a specific test consisting in a short statistical proof. It was used for better comparison and testing DNNs, before selection for application in the APF control. The statistical proof consisted in the generation of a new set of synthetically distorted waveforms, different from the patterns in the training and validation datasets, and the computation of some statistical measures of the errors made by the NN predictions:

- Mean error
- Mean absolute error
- RMSE
- Absolute error percentile 95
- Absolute error percentile 99
- Absolute error maximum

The most representative measure is the mean absolute error, MAE, (29),

$$MAE = \frac{1}{N}\sum_{i=1}^{N}\left|\hat{a}_i - a_i\right| \tag{29}$$

where a_i is the actual value, $\hat{a}_i$ is the network prediction, and N is the number of waveforms, chosen as 10 thousand. The a_i variable states for coefficients A_1 or B_1. Their absolute values range from 0 to 1.5.

Once the best 80-cell LSTM was chosen, the training process was repeated with GRU networks. Again, a simple structure containing one GRU layer was the best choice, and a cell number around 80 yielded the best results. Table 4 presents the statistical error measures comparison. From the MAE = 0.0029 for LSTM, and MAE = 0.0081 for GRU, it may be inferred that the best option is the first one. The different results in Table 4 illustrate a better error distribution in the LSTM predictions.

TABLE 4. Error analysis with 10k waveforms for best FCE by LSTM and GRU.

	Error LSTM 80 cells		Error GRU 80 cells	
Error measure	A_1	B_1	A_1	B_1
mean error	−0.00004	0.00006	0.00015	−0.00019
MAE	0.0029	0.0027	0.0081	0.0079
RMSE	0.0040	0.0038	0.0101	0.0096
abs. percentile-95	0.0080	0.0073	0.0196	0.0168
abs. percentile-99	0.0137	0.0133	0.0308	0.0289
abs. maximum	0.0226	0.0229	0.0373	0.0351

B. TRAINING THE NN FOR FREQUENCY ESTIMATION

Regarding the FE task, the description in the previous subsection allows to simplify this one. It should be noted that for the FE function the NN will have as input the voltage waveform, less distorted than the currents. Therefore, the training patterns did not need to include high levels of harmonic distortion. However, the objective requires a higher resolution in the different frequency values present in the patterns. The work in [30] described the feasibility of using a feedforward network for FE in sinusoidal signals under noise conditions. The disturbance by electrical signals is not the noise but the harmonic distortion.

The measurement or estimation of the frequency usually requires more than one cycle. Thus, some tests were carried out to select the convenient number of cycles for the learning data. As a compromise between performance and the lowest possible vector size, patterns with a length of 4 cycles were selected. Shorter time intervals produced a slightly lower accuracy, whereas longer times did not increase it. Therefore, the data contain 512 samples per pattern, corresponding to 80 ms time. The frequency sweep is 49.5-50.5 Hz. The set of training patterns has been generated using 101 frequency values distributed in the interval in steps of 0.01 Hz. For every frequency, 2000 waveforms were generated. The values of the coefficients A_1 and B_1 were selected exactly as in the previous section, but the harmonic distortion incorporated was much lower, comprising harmonic orders 3, 5 and 7, with coefficients A_i and B_i from the interval [−0.2,0.2]. The training arraydatastore had 202 thousand patterns. The targets were chosen as the (f-49.5) value. In this way the output range for the NN was [0,1], which is usually better for the neural network learning.

LSTM and GRU networks were trained. The required training and network parameters were similar to the ones used by the FCE task, except for an optimum number of 30 cells, and 30-40 training epochs. The input layer has a size of 512, and the fully-connected layer only one element.

The final validation RMSE in the best training with LSTM was 0.035 (Loss = 0.0006). The GRU network obtained RMSE = 0.032 (Loss = 0.0005). Although it does not seem to be a significant difference between both models, in the multiple training runs, the GRU network always obtained a lower error. After the trainings, a statistical proof has been applied as a generalization and performance test with 10k waveforms. Table 5 presents the comparative results models in terms of error analysis.

TABLE 5. Error analysis with 10k waveforms for best FE by LSTM and GRU.

Error measure	Freq. error LSTM 30 cells	Freq. error GRU 30 cells
mean error	−0.0009	0.0003
MAE	0.0177	0.0122
RMSE	0.0393	0.0199
abs. percentile-98	0.0544	0.0306

From the error analysis in table 5, it is clear that the GRU network outperforms the LSTM. The most significant index is the MAE, whose value for the GRU is approximately 0.01 Hz. The absolute error percentile-98 of 0.03 Hz shows that, in general, higher FE errors are not expected. Moreover, the mean error is practically zero, and the application of the network to the APF control will give updates every 20-ms. Therefore, the effects of the small errors in the generated waveforms during those short time intervals should not be

noticeable. This will be better evaluated in the following sections with simulation and experimental results.

V. RESULTS OF PRACTICAL CASES BY SIMULATION

A 3-phase system with shunt APF has been implemented in the Simulink environment for a thorough evaluation of the control method. Fig. 7 shows a diagram of the compensated power system, which will be described below.

A. SIMULATION PROCESS DESCRIPTION

The THD of the currents and the supply PF are the first factors of merit to be considered for performance evaluation of a compensation control. The definition of the THD index is given in (30),

$$THD = \frac{\sqrt{\sum_{i>1} I_i^2}}{I_1} \cdot 100\% \tag{30}$$

where I_i is the *rms* value of each current harmonic, and I_1 corresponds to the fundamental one. The definition of the PF is provided in (31),

$$PF = \frac{P}{3V_e I_e} \tag{31}$$

where P is the active power, and V_e, I_e represent the effective values of the three-phase voltages and currents according to IEEE Std 1459, [32]. Apart from those two indices, other relevant parameters to evaluate the compensation results are the active and reactive powers, and the *rms* value of the line currents, comparing them before/after compensation.

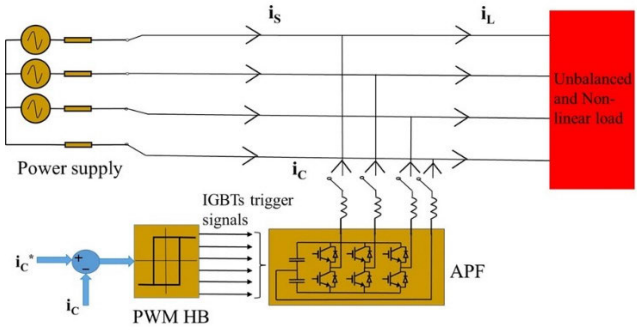

FIGURE 6. Three-phase power system with neutral wire compensated with an APF by hysteresis band PWM control (PWM HB).

On the basis of the shunt APF simplified schematic in Fig. 6, the Simulink model was implemented as shown in Fig. 7, with parameters in Table 6. The reference currents controller is divided into two parts. The first subsystem contains the LSTM and GRU networks for FCE and FE. The second one contains the computing operations generating the active currents from the estimated coefficients and frequency, according to the proposed method, illustrated in Fig. 2. The active currents correspond to the expression in (17). The subtraction in (18) between load and active currents is carried out inside the APF subsystem of Fig. 7 to obtain the compensation reference currents.

The use of the NNs with currents and voltages of practical three-phase circuits requires the application of a scale factor to adapt their values. The NN input signals should not much exceed the amplitudes managed in the training phase. For the voltage, it is easy to fix a suitable scaling factor, but the current magnitude highly depends on the load features. A solution may be adjusting an appropriate factor for the maximum expected currents.

Nevertheless, this is no critical issue, because of the wide tolerance observed by the LSTM, regarding the input signal amplitude. It has shown a good generalization capability in the different tests.

TABLE 6. System parameters for simulation.

Parameter	Value
Supply voltage, nominal frequency	400 V, 50 Hz
Passive filter	L = 12 mH
Capacitors	C = 2.2 mF
V_{DC} ref. (V_{DC1}, V_{DC2})	400 V, –400 V
Sampling frequency	6.4 kHz
Thyristors-RL loads case 1	Load1: 72º, 40 Ω, 30 mH
(firing angle, R, L)	Load2: 117º, 28 Ω, 16 mH
Thyristors-RL loads case 2	Load1: 72º, 40 Ω, 35 mH
	Load2: 153º, 6 Ω, 5 mH
Thyristors-RL loads case 3	Load1: 95º, 22 Ω, 24 mH
	Load2: 153º, 24 Ω, 3 mH

Inside the first control subsystem the 6 sampled waveforms of voltages and load currents are used for the FCE by means of the LSTM network. The figure shows detail of the 'LSTM A B predict' Simulink block containing the LSTM operation. Every 20 ms the LSTM updates the 12 coefficients A_i and B_i. The FE is carried out by the GRU network applied to one phase voltage. The detail in the bottom-right of Fig. 7 shows the 'GRU freq predict' block containing the GRU operation. Its output consists in the estimation of the (f−49.5) value, as explained in Section IV, because of the training method followed to achieve higher accuracy. Therefore, in Fig. 7 a constant 49.5 value is added to the GRU output to obtain the frequency. The GRU input is a 4-cycle signal interval taken as a running window, providing input updates every 20 ms. The phase ωt for the sine and cosine functions in (18) is computed from the frequency as described in (20) and in Fig. 3.

Table 6 contains the relevant system parameters. A 3-phase voltage source supplies the load currents at variable frequency. The passive filter in the converter output branch has a series inductance of 12 mH (in Fig. 7 it is located inside the "APF" subsystem). The hysteresis band control for the converter PWM has a switching threshold of ±0.03. And the sampling rate for voltages and currents is set to 6.4 kHz. There are two parallel three-phase loads. In particular, two three-phase thyristor-regulators with different firing angles and RL parameters in each branch have been used. This load array enables a wide variety of different load currents.

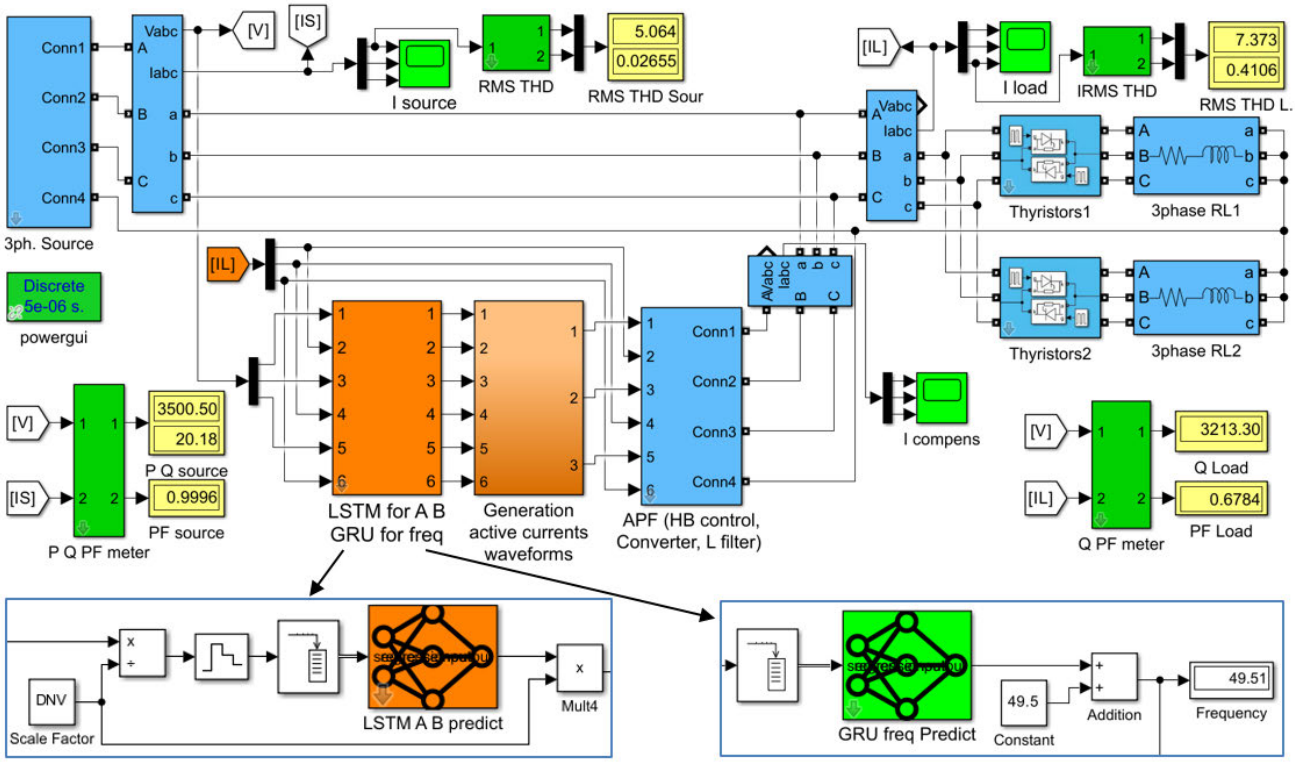

FIGURE 7. MATLAB-Simulink model used for tests with practical cases. It shows the results after simulation of Case 1a (see Table 7). Bottom left, detail of the FCE-LSTM predict block. Bottom right, detail of the FE-GRU predict block.

Three cases have been selected for presentation of results, according to the parameters included in Table 6 as case 1, case 2 and case 3. The load parameters were selected aiming to obtain clearly different current waveforms, with high distortion levels and low PF values.

Furthermore, the condition of power supply frequency variation has been considered, by selecting two different frequency values for each case, all of them deviated from 50 Hz to test unfavourable conditions. Hence a total of six case studies are simulated, with the frequency values of Table 7.

B. COMPENSATION RESULTS

The compensation results are presented by means of 3 load configurations, with 2 different frequencies each. Table 7 contains the 6 practical cases of the study, beginning with Case 1a at 49.5 Hz, and ending with Case 3b at 50.5 Hz.

TABLE 7. Compensation results of the 6 practical cases. The frequency estimation (FE) is also included.

Case	Source f (Hz)	GRU FE (Hz)	Load THD(%)	Source THD(%)	Load PF	Source PF
Case 1a	49.5	49.51	41.1	2.6	0.68	> 0.99
Case 1b	50.1	50.12	41.3	2.7	0.67	> 0.99
Case 2a	49.7	49.71	48.9	3.6	0.57	> 0.99
Case 2b	50.3	50.30	46.7	3.8	0.58	> 0.99
Case 3a	49.9	49.90	51.2	4.2	0.53	> 0.99
Case 3b	50.5	50.49	51.6	4.0	0.52	> 0.99

Table 7 shows the source frequency of the 6 practical cases along with the results. Firstly, the FE obtained by the GRU network is included. The following columns illustrate the compensation results, in terms of current THD reduction and PF correction. Fig. 8 shows the load currents of three cases: Case 1a, Case 2a, and Case 3b.

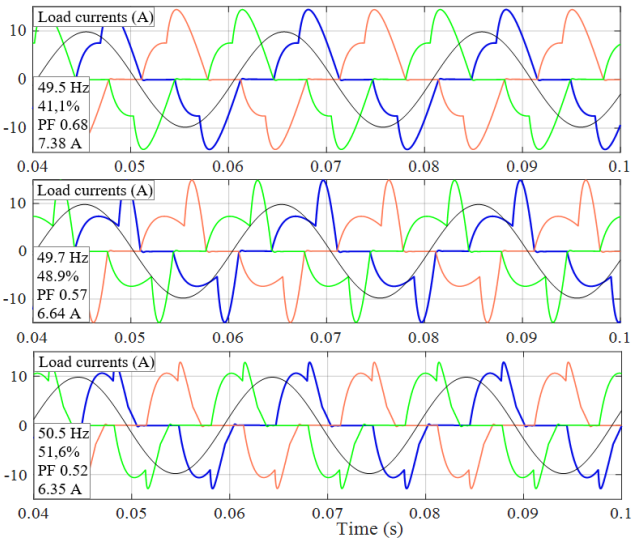

FIGURE 8. Load currents of three simulations: Case 1a, Case 2a and Case 3b. The graphs include the values of source frequency, current THD, PF and *rms* current, as well as ph. 1 scaled voltage waveform.

Analyzing the FE results in Table 7, the estimations yield values very close to the actual frequencies, with errors of the order of 0.01 Hz. This is consistent with the generalization test described in Section IV and Table 5. Regarding the distortion mitigation, the load THD ranges from 41% to 52%, and after compensation, their values drop to 2.6% - 4.2%, clearly under 5%. Finally, the last columns in the table show the PF correction, where the source PF was clearly over 0.99 in all cases.

Fig. 9 presents the resulting source and compensation currents after the APF connection in the Case 1a. The waveforms of source currents become sinusoidal, with THD = 2.6%. The reactive power compensation may be verified from the voltage and source current waveforms in the graph. The PF is almost unity, and the current drops from 7.38 A (Fig. 8) to 5.06 A (Fig. 9).

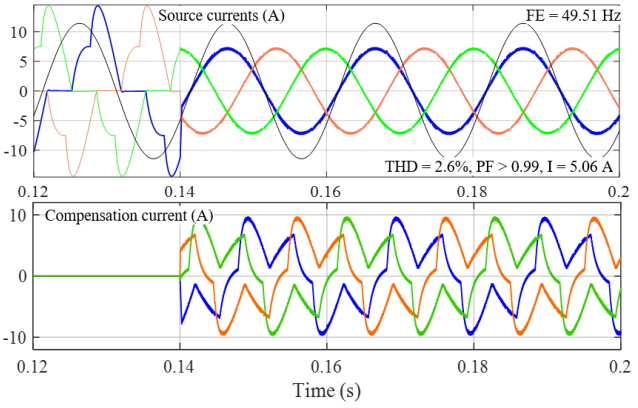

FIGURE 9. Results in Case 1a, f = 49.5 Hz. Source and compensation currents. Connection of the APF in t = 0.14 s. The ph.1 voltage waveform (scaled) is included for reference.

Fig. 10 contains the graphical results of the Case 3b, visualizing phase-1 current and voltage waveforms. The voltage is divided by a factor of 40. The source current shape clearly shows the distortion and reactive power compensations, causing the *rms* current decrease from 6.35 A to 3.39 A. In the bottom graph, it has been highlighted the zero-crossing of voltage and source current near 0.2 s, where the time instant is exactly 0.198 s, which is the corresponding instant time after 10 cycles for a 50.5 Hz frequency. It illustrates the correct function of the FE.

It must be remarked that the precise FCE and FE estimations carried out by the NNs are responsible for the good compensation results.

The dynamical behavior under load changes has been also evaluated. An example of load change and its effects on the compensation is presented, using the Case 2a. The connection at t = 0.135 s of an additional 3-phase RL load to the first set of thyristors has been implemented. Fig. 11 illustrates the results, including the load, source and compensation currents. A fast transient response is observed, taking between 1 and 2 cycles time, without specially altered current waveform during that time interval. The FCE and FE functions seem to

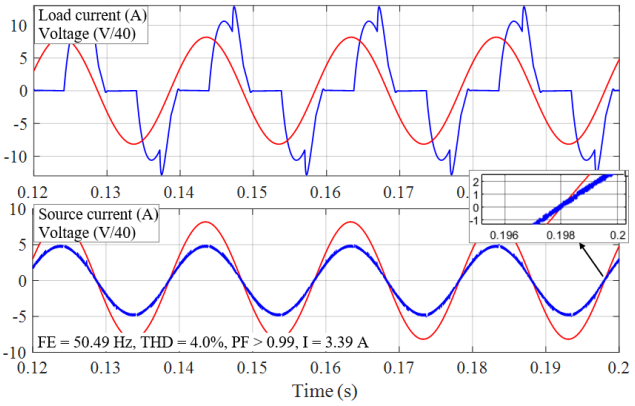

FIGURE 10. Results in Case 3b, with f = 50.5 Hz. Top: phase-1 load current and scaled voltage. Bottom: phase-1 source current and scaled voltage, with a zoom-in view of the zero-crossing near 0.2 s, that highlights the cross at t = 0.198 s according to the 50.5 Hz frequency.

work robustly during the cycles following the change, as no visible deviation of the period length can be appreciated, and a stable waveform can be observed after t = 0.16 s.

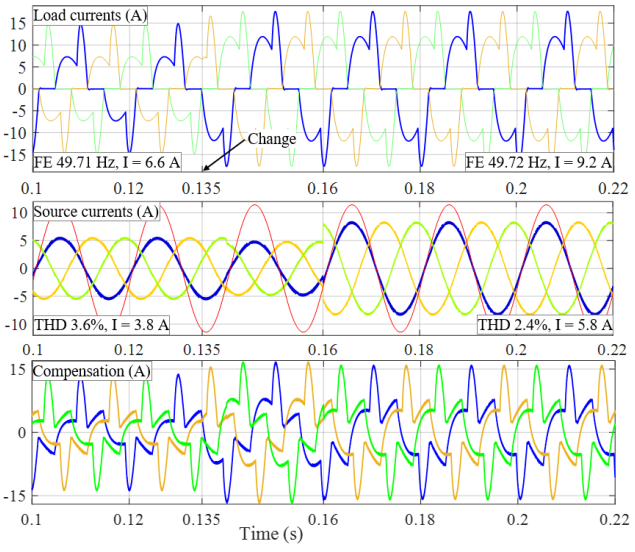

FIGURE 11. Load change in Case 2a, f = 49.7 Hz, at time t = 0.135 s. Load, source and compensation currents (ph. 1 scaled voltage for reference).

Finally, it follows a brief study of the NN generalization capabilities with frequencies beyond the training limits. The purpose is to reveal the behavior of both NNs when high grid frequency deviations occur. The training of both networks was made with frequencies within 49.5-50.5 Hz. A test with values outside that interval has been carried out, using the simulation model with load case 1. The results are presented in Table 8.

The results in Table 8 show that, despite the high frequency deviations, the control approach provides satisfactory compensation indices, and no malfunction is observed. It can be affirmed that both LSTM and GRU networks present a good

TABLE 8. Generalization test with high frequency deviations.

Source freq	FE (Hz)	Source THD	Source PF
49 Hz	48.95	2.6 %	> 0.99
51 Hz	51.04	2.8 %	> 0.99
48 Hz	47.42	3.1 %	> 0.98
52 Hz	52.26	3.0 %	> 0.99

generalization capability in these circumstances, allowing a robust function of the control.

VI. EXPERIMENTAL RESULTS AND DISCUSSION

The proposed method has been validated with a laboratory prototype of the shunt APF. The APF has been implemented based on a current-controlled voltage source inverter, CC-VSI. For use in three-phase four-wire systems, a three-leg inverter topology with a 'split capacitor' on the dc side was provided. In this way, the midpoint of the dc capacitors provides a fourth conductor in the VSI for return currents through the neutral conductor (zero sequence currents). On the other hand, a PWM (pulse width modulation) control by hysteresis band, HB, for switching the converter IGBTs was implemented, Fig. 6.

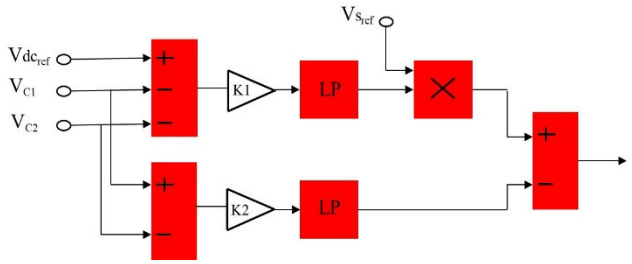

FIGURE 12. Block diagram for capacitor voltage control on the dc side of the APF inverter.

A voltage regulator for the purpose of maintaining the levels of the capacitor voltages on the dc side of the VSI has been developed, Fig. 12. In fact, the losses due to the converter tend to discharge capacitors C_1 and C_2 on the dc side. On the other hand, its operation in unbalance situations produces the circulation of zero sequence currents through the neutral wire. The last one, supposes the appearance of an unbalance in the values of the voltages of each capacitor. Voltage variations on the dc side, whether due to one cause or the other, can be corrected with proper power balancing from the supply source. Fig. 12 shows the schematic of the voltage regulator for the capacitors located on the dc side of the VSI. Both the sum of the voltages of the two capacitors and their difference are subtracted from a determined reference voltage. The resulting signals that collect the variations of the voltages over time at each capacitor are passed through two low-pass filters, LP. The LP filters select the dc components of the capacitor voltage variations and from these, together with the reference phase voltages of the mains voltages, form active current components that help to restore the power balance in the APF. This additional active current component is added to the active component corresponding to the load current; both constitute the active current supplied by the ac source.

Fig. 13 shows the experimental setup. A modular system has been used, containing dSPACE acquisition and control cards. It includes a DS1005 PPC control card with a PowerPC 750GX processor that executes the control program in real time. This card manages the inputs and outputs signals in the connections with the power system by means of two additional cards: a DS2004 card with 16 inputs, and a DS5101DWO card with 16 TTL type outputs. The input signals come from Hall effect LEM sensors for voltages (LV-25-P) and currents (LA35-NP). The three-phase power converter has a three-leg inverter with two capacitors on the DC side. The inverter is made up of Semikron SKM50GB123D modules, consisting each of two IGBTs. The MATLAB/Simulink model is executed, and a real-time interface tool enables the interaction and control. Regarding the interface branches between APF and network, and type of modulation control, the same values have been implemented as those used in the simulation model. More details on the experimental setup can be found in [2].

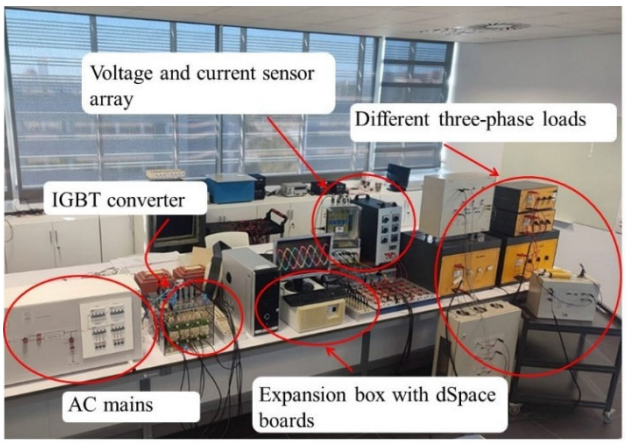

FIGURE 13. Experimental setup of the NN-based APF.

Several individual 3-phase loads connected in parallel in a Point of Common Coupling (PCC) have been chosen to test the shunt APF control in practical experiments. The connection is done through switches that allow to combine the individual loads to arrange different total load settings. Besides, some of the elements (R, L, C) in the individual loads can be changed. In the forthcoming descriptions the total settings will be called 'Loads'.

Variable configurations with the available individual loads provide different total loads in the system allowing an in depth testing of the proposal. The supply was the 400 V, 50 Hz distribution network, and the line connecting the PCC with the grid may include an optional series inductance.

The experimental practical cases have been named 'Load 1' to 'Load 8'. The load settings and parameters are described in Table 9 and Table 10. In the two following subsections, the results are presented, split into balanced and unbalanced experiments. In a last subsection, a comparative discussion is carried out.

A. BALANCED SYSTEM EXPERIMENTS

Here, six very different loads (Load 1 to Load 6) have been considered. Table 9 presents their parameters. The voltage in these tests is balanced and almost sinusoidal.

TABLE 9. Features of the balanced practical cases.

Total load case	Features of parallel loads combinations (grid supply 400 V, 50 Hz)
Load 1	3-ph. 6-pulse rectifier R_{DC} = 242 Ω
Load 2	3-ph. resistance, R = 120 Ω 3-ph. rectifier R_{DC} = 242 Ω
Load 3	3-ph. RL, R = 40 Ω, L = 0.3 H 3-ph. capacitors, C = 10 µF 3-ph. rectifier R_{DC} = 242 Ω
Load 4	3-ph. resist. R = 120 Ω; 3-ph. capacitors C=10 µF 3-ph. RL, R = 80 Ω, L = 0.2 H, 3-ph. rectifier R_{DC} = 242 Ω Additional line series inductor lowering the PF
Load 5	3-ph. RL, R = 80 Ω, L = 0.2 H, 3-ph. capacitors, C = 10 µF 3-ph. rectifier R_{DC} = 242 Ω
Load 6	3-ph. RL, R = 40 Ω, L= 0.35 H, 3-ph. rectifier R_{DC} = 130 Ω

A first step to present the results is summarized and self-contained in Fig. 14. The first four loads (Load 1 to Load 4) have been tested, inserting in the figure the load currents waveforms along with the THD and PF values before/after compensation (load/source). The graphs include a scaled voltage waveform of one of the phases for better comprehension of the load features. Each case also presents the frequency value resulting from the FE obtained by the GRU network. Afterwards, in the following figures the detailed results of Load 5 and Load 6 will be presented.

These first results in Fig. 14 show the operation of the control with 4 loads, obtaining low source distortion and PF practically one. The frequency estimations included in the graphs show values very close to 50 Hz.

Fig. 15 shows detailed results of the Load 5 case. Here, the 3-phase voltages are presented along with the load and source currents. The load currents graph includes the THD, PF and *rms* current before compensation. The source currents graph includes the results after compensation, where the distortion mitigation and the PF correction can be clearly observed. Note that the source current shapes are sinusoidal, in spite of the slight distortion observed in the voltages. As it was justified in Section II, the method uses the fundamental voltage components to generate the APF reference signals. Hence, the control always tends to produce sinusoidal waveforms.

Detailed results of the Load 6 are presented in Fig. 16, containing the load, compensation and source current waveforms

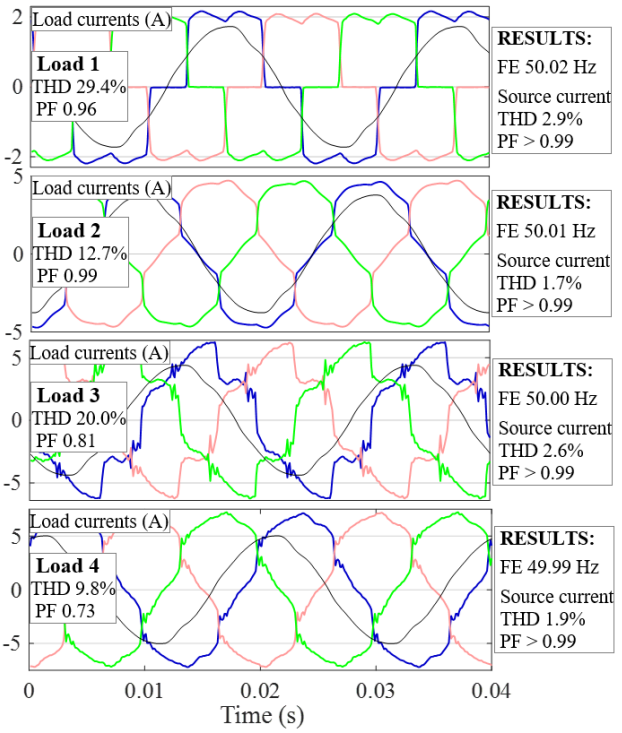

FIGURE 14. Load currents of Load 1, Load 2, Load 3 and Load 4, including a view of one scaled voltage. At the right of each graph: The FE and compensation results.

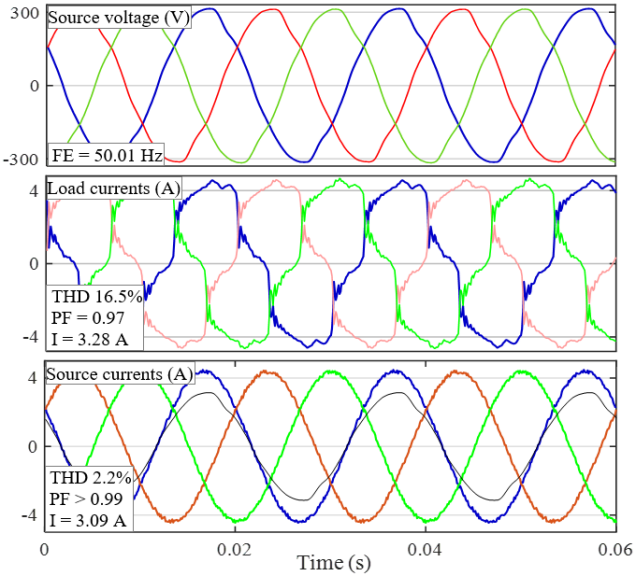

FIGURE 15. Load 5 results. Source voltage, load currents, source currents (with one scaled voltage) and compensation results.

along with the performance indices and harmonic spectrum before/after compensation. The source current graph includes the scaled phase voltage waveform to highlight the reactive power compensation. The current THD drops from 20% to a very low 2.3% value, and the spectrum graphs verify this

harmonic mitigation showing the very low harmonic content after compensation.

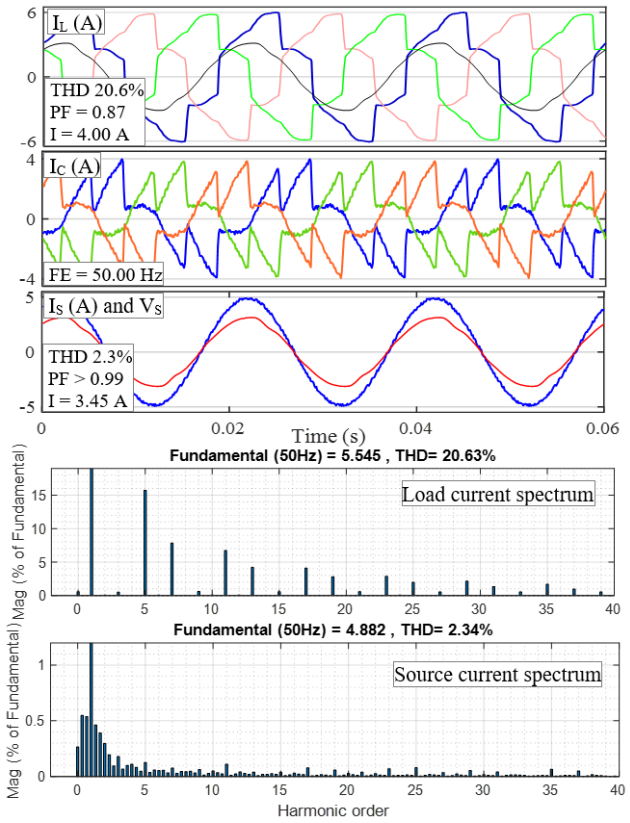

FIGURE 16. Load 6 results. Load, injected and source currents, including the THD, PF and FE values. Bottom: Harmonic spectrums before/after compensation.

TABLE 10. Features of the unbalanced practical cases.

Setup name	Features of parallel loads combinations
Load 7	Balanced grid voltage supply. 3-ph. unbalanced load: R_1 = 90 Ω, R_2 = 138 Ω and single-phase rectifier in phase 3. 3-ph. 6-pulse rectifier R_{DC} = 242 Ω
Load 8	Unbalanced voltage programmable source 3-ph. balanced RL, R = 80 Ω, L = 0.2 H, 3-ph. balanced capacitors, C = 20 µF 3-ph. 6-pulse rectifier R_{DC} = 242 Ω

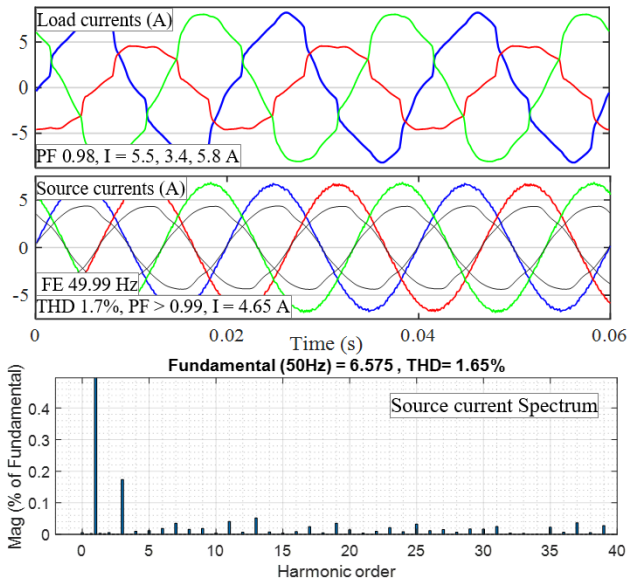

FIGURE 17. Load 7 case. Balanced voltage unbalanced load. Load and source currents, including compensation indices and the source current spectrum.

B. UNBALANCED CONDITIONS

The present control approach tackles the problem of unbalanced load currents. Under balanced voltage supply conditions, the active current waveforms provided by the control system should be balanced, according to (10). Hence the source currents after compensation should become also balanced. However, in case of unbalanced voltage supply it should achieve only harmonic removal and power factor correction.

Two different unbalanced conditions have been tested. Table 10 shows the main features of the experimental arrangements, where Load 7 is an unbalanced load setup connected directly to the grid, whereas Load 8 corresponds to a system supplied by a programmable source presenting unbalanced voltage and considerable harmonic distortion.

The Load 7 results in Fig. 16 prove another outstanding compensation characteristic of the proposal. It yields PF correction along with balanced and sinusoidal currents, whose low 1,7% THD value can be verified in the scarce harmonic contents of the provided spectrum.

On the other hand, the last experimental test reveals the behavior under severe unfavorable conditions. The distorted and unbalanced voltage supply of the arrangement called Load 8 is shown in Fig. 18. The control enables the harmonic and PF correction, although the source currents present imbalance, which is a drawback of the method.

Finally, it must be highlighted that the FE values obtained in the 8 experimental loads presented in this section were between 49.99 and 50.02 Hz. The frequency was not measured by means of a precision instrument for comparison, but these estimations so close to 50 Hz, combined with the general high performance in terms of compensation, confirms the correct operation.

C. COMPARATIVE DISCUSSION

A comparative analysis and discussion has been carried out. The aim of this work is not to prove a general highest performance compared to other techniques. Some APF control publications demonstrate very efficient behavior and complete description and testing, as the SGF proposal in [8], although generally some drawbacks may be found in most papers.

In the case of the NN control methods, that are promising since long ago, some shortcomings may be observed in all

TABLE 11. Comparison of some important features among different APF NN-control publications.

Relevant feature	[12]	[13]	[14]	[17]	[19]	[26]	[27]	FCE-FE
NN type	Adaline	Adaline	Adaline	RNN	MLP	GRU	LSTM	LSTM GRU
Adaptive algorithm	adaptive	adaptive	adaptive	adaptive	prev-train	prev-train	prev-train	prev-train
Training description	-	-	-	-	fully	no	no	fully
PLL required	no	no	PLL	no	PLL	not clear	not clear	no
Compensation harm. + PF	yes THD > 5%	only harmonic	only harmonic	yes	yes	yes	yes	yes
Balanced source currents	yes	no	somewhat	with balanced V	with balanced V	not clear	yes	with balanced V
Sim./experim. cases	both, scarce	both	both	both	both	only sim.	only sim.	both
Test different loads	scarce	scarce	acceptable	acceptable	yes	acceptable	acceptable	yes
Robust frequency deviations	not clear	yes, tested	yes	not clear	yes, tested	not clear	not clear	yes, tested

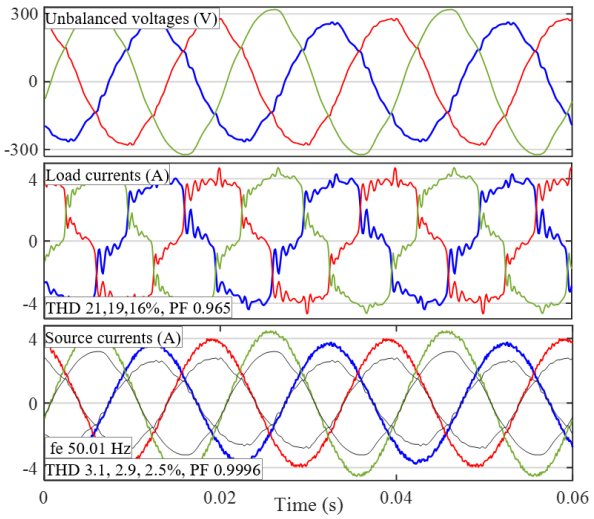

FIGURE 18. Unbalanced and distorted supply voltage in Load 8 case. The control achieves harmonic and PF correction.

publications. This paper aims to provide a complete description and a thoroughly tested method, based on previous trained NNs, that neither requires the permanent computation of an adaptive algorithm nor an additional PLL control.

We have reviewed many NN control publications and selected several notable works that provide more or less complete 3-phase compensation characteristics. In Table 11 a comparison is shown, in terms of different relevant features regarding the method or the publication itself:

- Adaptive algorithm or previous training.
- Training description, in case of previous trained NN.
- PLL required: the need of additional PLL control.
- Compensation of both harmonics and PF.
- Balanced source currents achieved or not.
- Simulation and experimental practical cases.
- Testing different loads or different conditions.
- Robust to frequency deviations, not always secured.

Regarding balanced currents, it can be 'generally accomplished' or 'only under balanced voltage conditions'. As regards the testing with different practical loads and conditions, despite the known constraints on the journal articles number of pages, it is convenient to test more than one practical load or different conditions. Some papers present very scarce practical testing.

The contents of Table 11 reveal interesting outcomes. None of the publications comply satisfactorily with the analyzed feature requirements. The work in [12] addressed the harmonic and PF compensation, but it does not show sufficient harmonic correction, presenting THD not below 5%, and it includes scarce practical case testing. The Adaline publications in [13] and [14] address only harmonic mitigation, among other weaknesses. In [17], a RNN high complexity iterative algorithm is applied, the balanced currents depend on the voltage conditions, and the behavior under frequency deviation is not clear.

The MLP proposal in [19] needs the additional PLL control, and the imbalance correction depends on the voltage. The works based on GRU [26] and LSTM [27] do not include any description of the NN training process, and are limited to simulated cases. Moreover, the need of PLL and the behavior under frequency deviations are not clear.

In conclusion, it is apparent that further improvement is possible and convenient. The present proposal satisfies those requirements, except for the disadvantage of balanced currents dependent on the balanced voltage. Therefore, this paper should mean a step forward in the field of neural controllers.

On the other hand, as compared with any other techniques in the literature, this proposal provides good general results in terms of most relevant indices and features, like very low THD (below 2-3%), unity PF, robustness under unfavorable voltage waveform conditions, or dynamical behavior. In terms of general performance, it provides many of the efficient features of the approaches in [8], [10], and [11], and it could be an alternative method. Although further thorough comparison should be made in future work.

VII. CONCLUSION

In this research work, a new control strategy has been proposed and tested for three-phase active power filters (APF), based on the potential provided by Deep Learning (DL) techniques. The relevance of suppressing electrical disturbances

justifies the efforts to develop new efficient control algorithms for the APF control. Despite the existence of many control techniques, the NN-based proposals generally present significant shortcomings. Therefore, in this work, a new neural controller is presented for further improvement. It consists in the use of two trained DL networks obtaining the full necessary information from voltages and currents to generate the APF reference waveforms. One of them undertakes the fundamental Fourier coefficients estimation (FCE), and the other produces a frequency estimation (FE). A simple computation process, without need of the conventional p-q or d-q transformations, achieves the reference currents, for compensation of harmonics and reactive power. The previously trained NN, due to its typical low latency feature and that it does not need an adaptive algorithm, requires less computation burden than the usual adaptive NN solutions. The novel FE function involved allows to fulfil the control without need of additional phase-locked loop (PLL) technique.

The long short-term memory (LSTM) and the gated recurrent unit (GRU) networks have been used for FCE and FE. Detailed description of the training method is reported. The LSTM accurately extracts the fundamental coefficients of voltage and current waveforms. The GRU estimates the grid frequency providing high accuracy of ± 0.01 Hz in the recommended interval $50 \pm 1\%$ Hz (IEC 61000-4-30 standard). The proposal has been thoroughly tested by many practical nonlinear loads and conditions both in simulation and with an experimental APF prototype. It provided high compensation performance, with generally low source current THD below 3% and unity power factor, with a robust behaviour under different conditions. The currents imbalanced is corrected, but only under balanced voltage. Comparing the FCE-FE proposal to other NN-controllers a considerable progress is observed, and it could be an alternative to other good techniques.

REFERENCES

[1] H. Akagi, E. Watanabe, and M. Aredes, "Shunt active filters," in *Instantaneous Power Theory and Applications to Power Conditioning*, 2nd ed., New York, NY, USA: Wiley, 2017, ch. 4, pp. 111–236.

[2] P. Salmerón, S. Pérez, and J. Prieto, "Shunt active power filter," in *Active Power Line Conditioners: Design, Simulation and Implementation for Improving Power Quality*. Amsterdam, The Netherlands: Elsevier, 2016, ch. 4, pp. 107–146.

[3] R. A. D. Oliveira and M. H. J. Bollen, "Deep learning for power quality," *Electr. Power Syst. Res.*, vol. 214, Jan. 2023, Art. no. 108887.

[4] M. Khodayar, G. Liu, J. Wang, and M. E. Khodayar, "Deep learning in power systems research: A review," *CSEE J. Power Energy Syst.*, vol. 7, no. 2, pp. 209–220, Mar. 2021, doi: 10.17775/CSEEJPES.2020.02700.

[5] Y. Hoon, M. Mohd Radzi, M. Hassan, and N. Mailah, "Control algorithms of shunt active power filter for harmonics mitigation: A review," *Energies*, vol. 10, no. 12, p. 2038, Dec. 2017, doi: 10.3390/en10122038.

[6] Y. Hoon, M. A. Mohd Radzi, M. A. A. Mohd Zainuri, and M. A. M. Zawawi, "Shunt active power filter: A review on phase synchronization control techniques," *Electronics*, vol. 8, no. 7, p. 791, Jul. 2019, doi: 10.3390/electronics8070791.

[7] J. Baros, V. Sotola, P. Bilik, R. Martinek, R. Jaros, L. Danys, and P. Simonik, "Review of fundamental active current extraction techniques for SAPF," *Sensors*, vol. 22, no. 20, p. 7985, Oct. 2022, doi: 10.3390/s22207985.

[8] K. Hasan, M. M. Othman, S. T. Meraj, S. Mekhilef, and A. F. Abidin, "Shunt active power filter based on savitzky-Golay filter: Pragmatic modelling and performance validation," *IEEE Trans. Power Electron.*, vol. 38, no. 7, pp. 8838–8850, Jul. 2023, doi: 10.1109/TPEL.2023.3258457.

[9] M. Tahir and S. K. Mazumder, "Improving dynamic response of active harmonic compensator using digital comb filter," *IEEE J. Emerg. Sel. Topics Power Electron.*, vol. 2, no. 4, pp. 994–1002, Dec. 2014.

[10] R. Panigrahi and B. Subudhi, "Performance enhancement of shunt active power filter using a Kalman filter-based H_∞ control strategy," *IEEE Trans. Power Electron.*, vol. 32, no. 4, pp. 2622–2630, Apr. 2017.

[11] M. Badoni, A. Singh, and B. Singh, "Comparative performance of Wiener filter and adaptive least mean square-based control for power quality improvement," *IEEE Trans. Ind. Electron.*, vol. 63, no. 5, pp. 3028–3037, May 2016.

[12] P. Salmeron and J. R. Vazquez, "Practical design of a three-phase active power-line conditioner controlled by artificial neural networks," *IEEE Trans. Power Del.*, vol. 20, no. 2, pp. 1037–1044, Apr. 2005.

[13] M. Sujith and S. Padma, "Optimization of harmonics with active power filter based on ADALINE neural network," *Microprocessors Microsyst.*, vol. 73, Mar. 2020, Art. no. 102976.

[14] S. Sharma, V. Verma, and R. K. Behera, "Real-time implementation of shunt active power filter with reduced sensors," *IEEE Trans. Ind. Appl.*, vol. 56, no. 2, pp. 1850–1861, Mar. 2020, doi: 10.1109/TIA.2019.2957734.

[15] P. Ch. Tah, A. K. Panda, and B. P. Panigrahi, "Shunt active filter based on radial basis function neural network and p-q power theory," *Int. J. Power Electron. Drive Syst.*, vol. 8, no. 2, p. 667, Feb. 2017, doi: 10.11591/ijpeds.v8.i2.pp667-676.

[16] M. Badoni, B. Singh, and A. Singh, "Implementation of echo-state network-based control for power quality improvement," *IEEE Trans. Ind. Electron.*, vol. 64, no. 7, pp. 5576–5584, Jul. 2017, doi: 10.1109/TIE.2017.2677359.

[17] H. Wang and J. Fei, "Nonsingular terminal sliding mode control for active power filter using recurrent neural network," *IEEE Access*, vol. 6, pp. 67819–67829, 2018, doi: 10.1109/ACCESS.2018.2878892.

[18] M. Qasim and V. Khadkikar, "Application of artificial neural networks for shunt active power filter control," *IEEE Trans. Ind. Informat.*, vol. 10, no. 3, pp. 1765–1774, Aug. 2014, doi: 10.1109/TII.2014.2322580.

[19] J. L. Flores-Garrido, P. Salmerón, and J. A. Gómez-Galán, "Nonlinear loads compensation using a shunt active power filter controlled by feed-forward neural networks," *Appl. Sci.*, vol. 11, no. 16, p. 7737, Aug. 2021.

[20] R. Gong and T. Ruan, "A new convolutional network structure for power quality disturbance identification and classification in micro-grids," *IEEE Access*, vol. 8, pp. 88801–88814, 2020, doi: 10.1109/ACCESS.2020.2993202.

[21] C. Pavlatos, E. Makris, G. Fotis, V. Vita, and V. Mladenov, "Enhancing electrical load prediction using a bidirectional LSTM neural network," *Electronics*, vol. 12, no. 22, p. 4652, Nov. 2023, doi: 10.3390/electronics12224652.

[22] N. Severoglu and O. Salor, "Amplitude and phase estimations of power system harmonics using deep learning framework," *IET Gener., Transmiss. Distrib.*, vol. 14, no. 19, pp. 4089–4096, Oct. 2020, doi: 10.1049/iet-gtd.2019.1491.

[23] N. Severoglu and Ö. Salor, "Statistical models of EAF harmonics developed for harmonic estimation directly from waveform samples using deep learning framework," *IEEE Trans. Ind. Appl.*, vol. 57, no. 6, pp. 6730–6740, Nov. 2021, doi: 10.1109/TIA.2021.3114127.

[24] E. Balouji, Ö. Salor, and T. McKelvey, "Deep learning based predictive compensation of flicker, voltage dips, harmonics and interharmonics in electric arc furnaces," *IEEE Trans. Ind. Appl.*, vol. 58, no. 3, pp. 4214–4224, May 2022, doi: 10.1109/TIA.2022.3160135.

[25] L. Liu, J. Fei, and C. An, "Adaptive sliding mode long short-term memory fuzzy neural control for harmonic suppression," *IEEE Access*, vol. 9, pp. 69724–69734, 2021, doi: 10.1109/ACCESS.2021.3077646.

[26] A. Ali, A. U. Rehman, A. Almogren, E. T. Eldin, and M. Kaleem, "Application of deep learning gated recurrent unit in hybrid shunt active power filter for power quality enhancement," *Energies*, vol. 15, no. 20, p. 7553, Oct. 2022, doi: 10.3390/en15207553.

[27] M. Iqbal, M. Jawad, M. H. Jaffery, S. Akhtar, M. N. Rafiq, M. B. Qureshi, A. R. Ansari, and R. Nawaz, "Neural networks based shunt hybrid active power filter for harmonic elimination," *IEEE Access*, vol. 9, pp. 69913–69925, 2021, doi: 10.1109/ACCESS.2021.3077065.

[28] *Electromagnetic Compatibility (CEM). Part 4–30, Testing and Measurement Techniques-Power Quality Measurement Methods*, Standard 61000-4-30:2015, IEC, 2015.
[29] *Voltage Characteristics of Electricity Supplied by Public Electricity Networks*, EN Standard 50160:2022, EN, 2022.
[30] H. R. Almayyali and Z. M. Hussain, "Deep learning versus spectral techniques for frequency estimation of single tones: Reduced complexity for software-defined radio and IoT sensor communications," *Sensors*, vol. 21, no. 8, p. 2729, Apr. 2021, doi: 10.3390/s21082729.
[31] J. Chung, C. Gulcehre, K. H. Cho, and Y. Bengio, "Empirical evaluation of gated recurrent neural networks on sequence modeling," in *Proc. Adv. Neural Inf. Process. Syst.*, 2014, pp. 1–24.
[32] *IEEE Standard Definitions for the Measurement of Electric Power Quantities Under Sinusoidal, Nonsinusoidal, Balanced, or Unbalanced Conditions*, Standard 1459–2010, 2010.

JUAN L. FLORES-GARRIDO was born in Moguer, Huelva, Spain. He received the Physics degree (specializing electronics) from the University of Seville, Spain, in 1994, and the Ph.D. degree from the School of Engineering, University of Huelva, Spain. From 1995 to 1997, he was a Product Engineer with Robert Bosch GmbH manufacturing plant, Spain. Since 2000, he has been an Associate Professor with the Department of Electrical Engineering, University of Huelva. He is currently a Researcher with Huelva Scientific and Technological Center (CCTH) and member with the Research Group Electrical and Electronics of La Rábida, GEYER. His lines of research are mainly focused on the electric power quality and the application of artificial neural networks and deep learning to the control of active power filters.

PATRICIO SALMERÓN was born in Huelva, Spain. He received the Ph.D. degree from the Electrical Engineering Department, University of Seville, Spain. Currently, he is with the Department of Electrical and Thermal Engineering, University of Huelva, where he is a Full Professor. He is a Researcher with Huelva Scientific and Technological Center (CCTH) and heads the Research Group Electrical and Electronics of La Rábida, GEYER. His lines of research have focused on the theory of electrical power in non-sinusoidal regimes, active power line conditioners, and the applications of artificial intelligence to electrical engineering. In this field, he has directed different research projects funded by competitive calls and has published a good number of papers in international journals.

JUAN A. GÓMEZ-GALÁN was born in Alosno, Huelva, Spain. He received the degree in electronic engineering from the University of Granada, Granada, Spain, in 1999, and Ph.D. degree (Hons.) from the School of Engineering, University of Seville, Spain, in 2003. He was an Invited Researcher with the Klipsch School of Electrical and Computer Engineering, New Mexico State University, Las Cruces, NM, USA, in Summer 2004. His current research interests include analog and mixed signal processing with emphasis on low-voltage, low-power implementations, and instrumentation systems in renewable energy systems. He is currently a Full Professor with the Department of Electronic Engineering, Computers and Automation, University of Huelva, Spain.

ALEJANDRO PÉREZ-VALLÉS was born in Arahal, Seville, Spain. He received the degree in industrial engineering from the University of Cádiz, Spain, and the Ph.D. degree from the School of Engineering, University of Huelva, Spain. He is currently the Head of the Department of Electrical Engineering and Thermal, Design and Projects, University of Huelva, where he has been an Associate Professor, since 1999. He is a Researcher with Huelva Scientific and Technological Center (CCTH) and a member with the Research Group Electrical and Electronics of La Rábida, GEYER. His lines of research have focused on electric power quality, design, and control of active power conditioners, with emphasis on the analysis and measurement of the quality of electrical power under conditions of asymmetry and distortion. Finally, he has participated in different research projects funded through competitive calls.